

Quantifying the nonlinear mode competition in the flow over an open cavity at medium Reynolds number

L. R. Pastur · F. Lusseyran · T. M. Faure ·
Y. Fraigneau · R. Pethieu · P. Debesse

Received: 29 August 2006/Revised: 8 October 2007/Accepted: 16 October 2007/Published online: 4 November 2007
© Springer-Verlag 2007

Abstract Our purpose is to quantify the rate of intermittency of nonlinearly competing modes, in a dominantly mode-switching scenario. What is the rate of presence of each mode? Can they simultaneously appear in, or disappear from the signal? The study is done in the context of open flows, exhibiting self-sustained oscillations, where air is here flowing over an open cavity. Reynolds numbers are of the order of 14,000. Velocity measurements downstream of the cavity are based on a laser Doppler velocimetry technique. We propose two methods to estimate the rate of presence of each mode: one based on a complex demodulation technique, the other on the distribution of the state vectors in the phase portrait of the signal.

1 Introduction

It is a remarkable fact that open flows such as jets, cavity flows, etc., may present spontaneous self-sustained oscillations. This is typical of an unstable configuration in which a preferred mode is selected and amplified (Rockwell and Naudascher 1979). In the case of flows past an open cavity, it has been observed, for medium and large Reynolds

numbers, some nonlinear competition between a few spectral components (usually two) (Rockwell 1983; Kegerise et al. 2004). The competition reveals to be dominated by a mode switching scenario, where one mode tends to prevent the rise of the other one, and reciprocally. Up to now, the physical mechanisms responsible for such a nonlinear competition has not been understood yet. In this article, we propose to focus on a quantitative analysis of the mode-switching phenomenon observed in the experimental flow over an open cavity at a moderate Reynolds number. The experimental setup and the mode-switching phenomenon are introduced in Sects. 2 and 3. Section 4 points out the fact that no mode-switching phenomenon is observed in a numerical flow, whose working parameters are similar to the experimental ones. To quantify the rate of existence of each competing mode, we introduce two different techniques. The first method is based on the complex demodulation of the time-signal, using the Hilbert transform (Sect. 5). In Sect. 6, existence rates are discussed with respect to three different threshold values. The second method is based on the dynamics phase portrait (Sect. 7). Both methods require to band-pass filter the signal around the spectral components under interest. A statistical analysis is conducted on the competing mode lifetimes in Sect. 8. Finally, a phase space first characterization is performed in Sect. 9, wondering about an underlying deterministic mechanism of the mode-switching phenomenon, before concluding in Sect. 10.

2 Experimental configuration

The system under study is a cavity of length $L = 10$ cm along the longitudinal x direction of the incoming air flow, height $H = 5$ cm along the vertical y direction (aspect ratio $R = L/H = 2$), and width $S = 30$ cm along the transverse z

L. R. Pastur (✉) · F. Lusseyran · T. M. Faure · Y. Fraigneau ·
R. Pethieu · P. Debesse
LIMSI-CNRS, BP 133, 91403 Orsay Cedex, France
e-mail: luc.pastur@limsi.fr

L. R. Pastur · R. Pethieu
Université Paris Sud XI, 91405 Orsay Cedex, France

T. M. Faure · P. Debesse
Université Pierre et Marie Curie, Paris VI,
75252 Paris Cedex 05, France

direction (Fig. 1b). The cavity is enclosed into a vein ($D + H = 12.5$ cm high). The origin of the axes in the (x, y) plane is taken at the upstream edge of the cavity, and midspan along the transverse z direction. The air flow is generated by a centrifugal fan placed upstream of a settling chamber (Fig. 1a). The incoming air flow is laminar and stationary, and the flow rate is kept constant during the experiment. The external velocity U_e is measured using laser Doppler velocimetry (LDV), 102 mm upstream of the cavity and 25.5 mm above the flat plate. This point of measurement is in the external flow sufficiently upstream of the cavity to avoid any perturbation from the instability developing above the cavity. At the wind tunnel outlet, the flow is rejected inside the experimental room. The reference flow velocity is $U_e = 2.09$ m/s (Reynolds number $Re_L = U_e L / \nu \simeq 14,000$). The measurement is performed over the x -component of the velocity downstream of the cavity, at point $x/L = 1.15$, $y/h = 0.33$, $z/l = 0$, using a LDV measurement. The time-series are acquired over 9 min, at a mean frequency rate of $f_c = 1,530$ Hz. The signal is re-sampled using a linear interpolation between the actual points of measurement, so as to provide regular time intervals of $\delta t = 1/f_c = 0.650$ ms. The time series is therefore constituted of about $N = 840,000$ points.

3 About the power spectral density

The power spectral density (psd) of the LDV signal exhibits two main components, that are not in an harmonic ratio (Fig. 2), the first spectral component (mode 1) at

$f_1 = 23.2$ Hz, the second (mode 2) at $f_2 = 31.0$ Hz. Their peak to peak ratio is $W_1/W_2 = 1.66$ (W_i being the power density in mode i). Other peaks appear as combinations of f_1 and f_2 , and harmonics. By construction, the psd only provides a statistical information on the spectral weight of each spectral component, composing the overall signal. It does not teach anything about the actual mode coexistence or exclusion in time. Indeed, the spectral density sensitively depends on the instantaneous mode amplitude, but also on its rate of presence over time. It may therefore happen that the most energetic modes in the psd only occur very episodically in time, in the LDV signal, but with an amplitude much larger than the amplitude of the other mode, so as to significantly contribute to the power spectrum.

To illustrate this point, a time–frequency representation of the signal has been plotted in the spectrogram of Fig. 3. There, the switching phenomenon between one spectral band, centred on f_1 , and a second spectral band centred on f_2 , clearly appears. Such a spectrogram should however be considered with some care, both axes t and f being reciprocally constrained by the uncertainty relation $\Delta t \cdot \Delta f = 1/2$, which means that the precision over one axis is inversely proportional to the precision over the second axis. Henceforth, the time localization of the switching events is directly related to the temporal sliding window width Δt used to perform the “instantaneous” Fourier transform at time t . In our case, $\Delta t \sim 10/f_1$ s, with a time step $\delta t = 112$ ms. Theoretically, it might be possible to extract the amplitude evolution of modes f_1 and f_2 by simply picking up the horizontal lines centred on f_1 and f_2 in the spectrogram. In practice, we will not use this technique, the

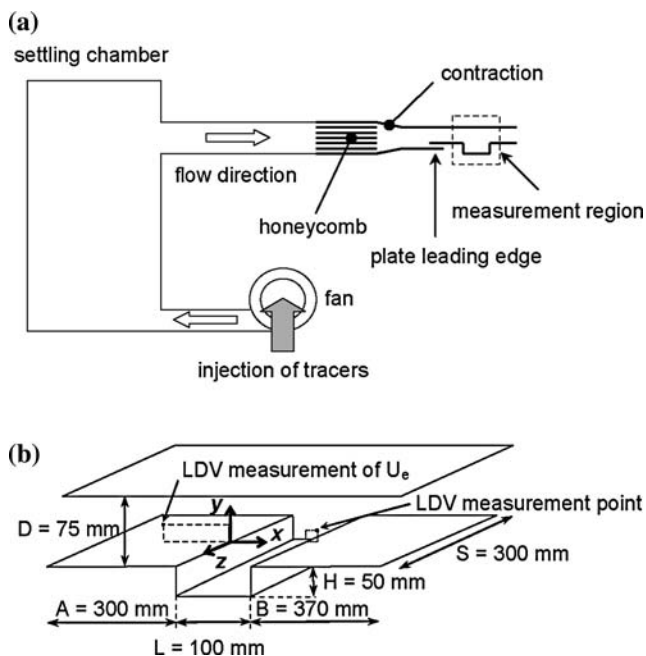


Fig. 1 Experimental setup. **a** Wind-tunnel principle; **b** cavity scheme

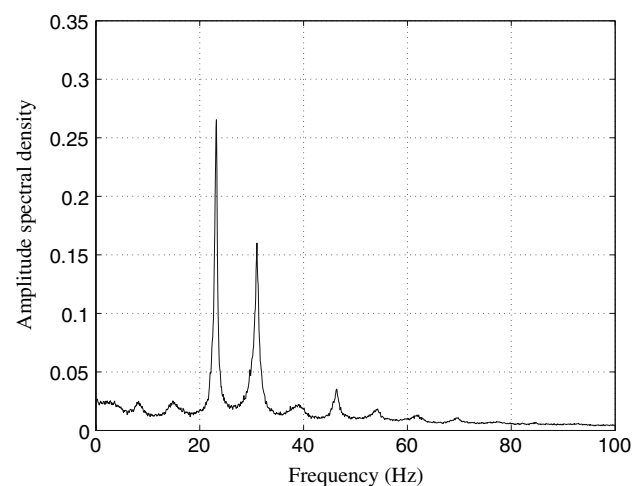
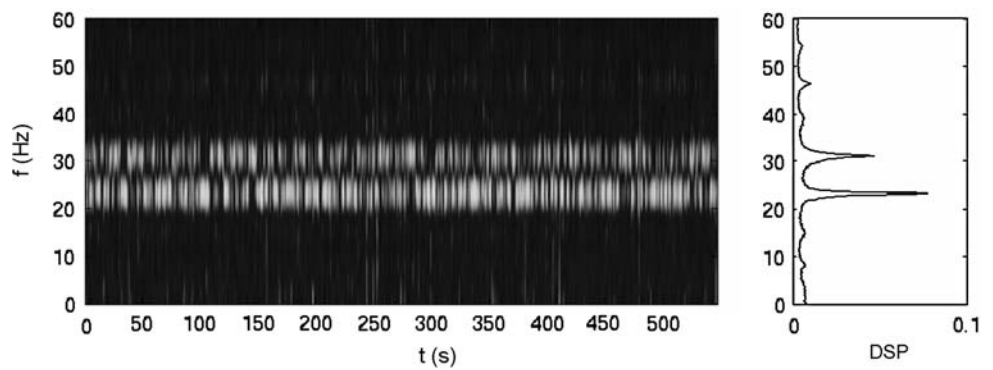


Fig. 2 Square root of the power spectral density, normalized to 1, of the LDV time series $s(t)$. Incoming flow velocity $U_e = 2.09$ m/s, aspect ratio $R = 2$. Two main modes emerge at $f_1 = 23.2$ Hz and $f_2 = 31.0$ Hz. The other peaks are nonlinear combinations of f_1 and f_2

Fig. 3 Spectrogram of the signal. The horizontal axis is the flowing time, the vertical axis the frequency space. Power spectral density is plotted as grey levels, from *dark* for small amplitude values to *bright* for larger amplitude values. The *right inset* is the time-integrated spectrogram



temporal resolution being three times larger than the slowest period $T_1 = 1/f_1$.

4 Mode-switching phenomenon in numerical simulation

Experimentally, the origin of such a mode switching phenomenon is not clearly understood yet. However, a 3D direct numerical simulation, carried out in our group, may bring some insights. The flow is assumed incompressible ($\nabla \cdot \mathbf{v} = 0$) and described by the Navier–Stokes equation

$$\frac{\partial \mathbf{v}}{\partial t} + \nabla \cdot (\mathbf{v}^t \mathbf{v}) = -\frac{1}{\rho_0} \nabla P + \nabla \cdot (v \nabla \mathbf{v}),$$

where t is the time, ρ_0 the uniform and constant density, P the pressure and v the constant kinematic viscosity (isothermal flow). The numerical method is similar to the one proposed in the framework of natural convection flow instability by Le Quéré et al. (1992) and Gadoin et al. (2001), and further applied to our open cavity flow (Podvin et al. 2006). Momentum equations are discretized following a finite volume approach on staggered structured grid with a second-order approximation in time and space. Scalar variables are defined at cell centres whereas vectorial variables are defined at cells boundaries. Advection fluxes are calculated with a QUICK scheme (Leonard 1979) and the viscous terms are defined with an usual second-order centred scheme. For stability reasons, the viscous fluxes are discretized using an implicit method. The incompressibility constraint ($\nabla \cdot \mathbf{v} = 0$) is guaranteed by a prediction/projection method, implying the resolution of a Poisson equation for the pressure updating.

The domain of simulation is similar to the experimental configuration shown in Fig. 1b. However, the spanwise direction is considered periodic and the length of the upstream cavity channel is reduced in order to save CPU time. The length of the domain is 400 mm, the width 200 mm and the height 125 mm. The inlet is located at the specific coordinate $x_0 = -110$ mm, the x -origin being located on the upstream edge of cavity. The inlet

conditions for the longitudinal velocity component are fixed such that the flow rate $U_q = 2.0$ m/s. It corresponds to the velocity profile of a laminar growing channel flow at the specific coordinate x_0 , calculated in a 2D channel flow simulation, which is in good agreement with the experiment. The other velocity component gradients are equal to zero. Usual nonsliding conditions are applied at the top and bottom walls. The domain is covered with 256 cells in the longitudinal direction, and 128 in the spanwise and normal directions. The mesh is particularly refined close to the walls and over the cavity, to well resolve upstream laminar boundary and stress layers and the eddy structures generated in the shear layer.

The numerical simulation is carried out over a time duration of 24.5 s, after the statistically converged flow has been reached out. The power spectral density of the signal picked up downstream of the cavity, at the same point of measurement as the experimental one, with a sampling frequency of $f_s = 454.5$ Hz, is shown in Fig. 4. The shear layer instability frequency is measured at $f_0 = 31.9$ Hz, close to $f_2 = 31.0$ Hz. No other mode of oscillation is

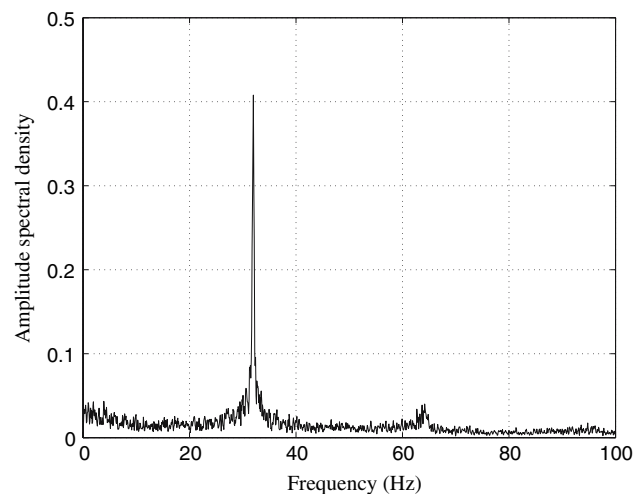


Fig. 4 Power spectral density in the 3D direct numerical simulations of the flow over an open cavity at the flow rate $U_q = 2$ m/s. Only one spectral component is present in the spectrum

however detected, meaning that the mode switching phenomenon is absent from the simulation. The reason for the discrepancy may teach us about the physical mechanism involved. First of all, note that although the numerical flow could be much more robust (with respect to environmental noise) than the experimental flow, which could let no chance to the other mode to develop, it remains that the cavity recirculation flow should be able to initiate, in the experimental flow as well as in the numerical one, strong enough perturbations in the upstream corner of the cavity to allow, at some time, the rise of the other mode. This is however not what happens. We may also wonder about the refinement of the mesh grid. But it appears that the highest frequency f_2 , which should be the less well-resolved one (since it is associated to smaller spatial structures), actually is resolved by the code, while the missing frequency is the lowest one f_1 . Henceforth, it is doubtful that the mesh grid may be responsible for the lack of mode switching phenomenon. Another possibility may lay in the numerical QUICK scheme under use, that could overdamp one of the two modes. In this respect, it may be useful to test a centred scheme. A last possibility for the discrepancy may lay in the transverse boundary conditions. They are rigid in the experiment, while they are periodic in the simulations. As a consequence, the recirculating secondary flows, in the transverse direction, symmetrically to the medium plane, as observed in the experiment, are absent in the simulations. How such secondary flows could induce the mode switching phenomenon is not obvious, but the possibility cannot be a priori excluded. A forthcoming campaign of simulations will be held with rigid boundary conditions, so as to mimic the experimental conditions, and should therefore bring more insights about the relevance of the boundaries in the mode switching phenomenon.

5 Complex demodulation

In this section, we propose to analyse more quantitatively the mode-switching phenomenon. It is necessary to

determine the instantaneous amplitude of each mode, at any time in the experimental time series. This is done using a complex demodulation technique on the basis of Hilbert transform. The method first requires to band-pass filter the signal around the spectral component under interest. This is done using a (noncausal) Butterworth filter of order 4. Mathematically, the Hilbert transform of a time-signal $s(t)$ is defined by the integral transform:

$$\mathcal{H}\{s(t)\} = \frac{1}{\pi t} * s(t), \quad (1)$$

where $*$ is the convolution product. In the Fourier space, it can equivalently write

$$\mathcal{F}\{\mathcal{H}\{s\}\} = -i, \operatorname{sgn}(\omega) \cdot \mathcal{F}\{s\}(\omega), \quad (2)$$

where \mathcal{F} is the Fourier transform operator, and $\operatorname{sgn}(\cdot)$ the sign function. The Hilbert transform therefore simply consists in rotating by $-\pi/2$ the positive part of the signal spectrum (multiplication by $-i = e^{-i\pi/2}$), by $+\pi/2$ its negative part (multiplication by $i = e^{i\pi/2}$). The Hilbert transform will therefore transform a cosine into a sine. As a consequence, it is possible to define an analytical signal $w(t)$ by

$$w(t) = s(t) + i\mathcal{H}\{s\}(t) \equiv A(t) \cdot e^{i\phi(t)}, \quad (3)$$

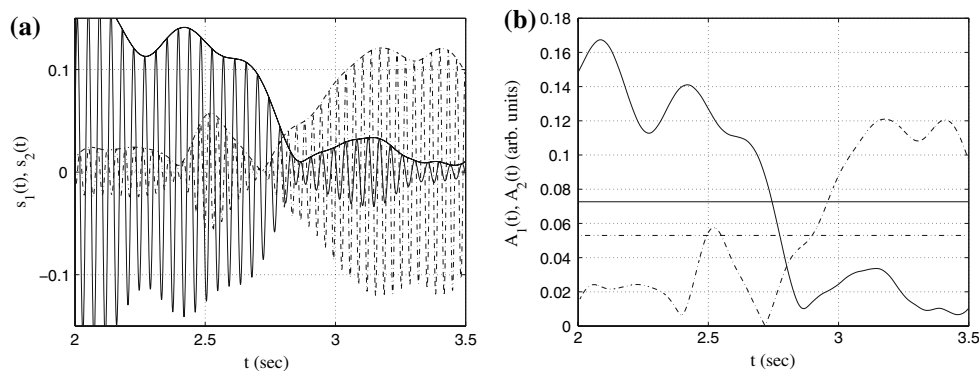
from which an amplitude $A(t)$ and a phase $\phi(t)$ can be derived, as

$$\begin{cases} A(t) &= |w(t)| \\ \tan \phi(t) &= \frac{\operatorname{Im}\{w\}}{\operatorname{Re}\{w\}} \end{cases} \quad (4)$$

The Hilbert transform is applied to the signals $s_1(t)$ and $s_2(t)$, obtained by band-pass filtering the LDV signal $s(t)$ around f_1 and f_2 , respectively. The resulting amplitudes $A_1(t)$ and $A_2(t)$, associated with $s_1(t)$ and $s_2(t)$, are plotted in Fig. 5 for an arbitrary time interval, where the mode switching phenomenon can be observed.

The mode-switching nature of the phenomenon is again confirmed by plotting A_2 with respect to A_1 (Fig. 6). It exhibits two compact clouds of points, one corresponding to A_1 saturating, A_2 vanishing, the other to A_2 saturating,

Fig. 5 Amplitudes $A_1(t)$ (solid line) and $A_2(t)$ (broken line) of modes f_1 and f_2 in signals $s_1(t)$ and $s_2(t)$, **a** with, or **b** without, the carrier. The threshold amplitudes \bar{A}_1 and \bar{A}_2 are plotted as horizontal solid and broken lines, respectively, in **b**



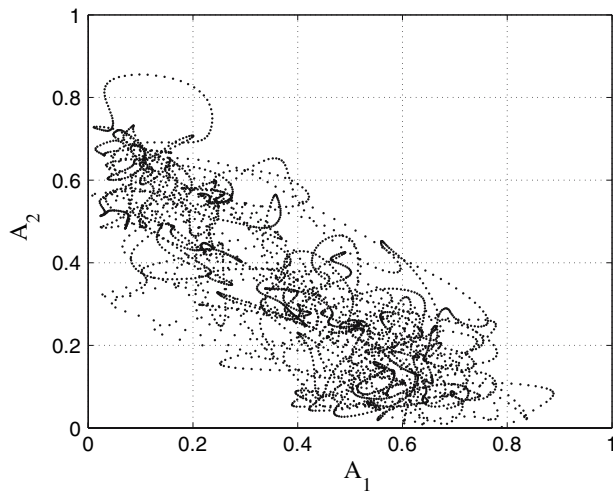


Fig. 6 Amplitude of mode 2 versus amplitude of mode 1, at any time

A_1 vanishing, with a more scattered cloud of points around the anti-diagonal when modes f_1 and f_2 are exchanging their stability, typical of an anti-correlated behaviour.

6 Criterion of existence

Now, we would like to determine the existence ranges of each mode f_1 and f_2 . For that, it is necessary to define a threshold value for the amplitude. A natural criterion is to compare the instantaneous mode amplitude $A_i(t)$ to the time averaged mode amplitude \bar{A}_i . For mode f_1 , $\bar{A}_1 = 0.073$, for mode f_2 , $\bar{A}_2 = 0.053$. At a given time t , the mode is considered present if $A_i(t) > \bar{A}_i$, absent unless. Defining t_i as the integrated time over which the mode f_i is present in the signal $s_i(t)$, we define the rate of

presence of the mode f_i as $\eta_i = t_i/T$, where T is the overall time of the signal. Following the criterion, it is found $\eta_1 = 0.524$, and $\eta_2 = 0.479$.

Noting that $\eta_1 + \eta_2 \approx 1.00$, one may conclude that the mode switching scenario is perfect, one mode being strictly present when the other is absent—and reciprocally. In fact, it appears that f_1 and f_2 are simultaneously present over $\eta_{\text{together}} = 6.8\%$ of the overall signal. It therefore follows that both modes must also be simultaneously absent from the LDV signal over a significant fraction of time, found to be $\eta_{\text{none}} = 6.5\%$. Henceforth, η_1 and η_2 also count common events. In Fig. 7 is shown an example in which both modes are seen simultaneously present in the signal (event of stability exchange, f_2 disappearing to the benefit of f_1).

Another natural threshold value can be defined, based on the mid-value A_{ic} between the largest and the smallest amplitude values:

$$A_{ic} = \frac{1}{2} \left(\max_t(A_i) + \min_t(A_i) \right). \tag{5}$$

This criterion has the benefit to well distinguish the existence range of a mode that would *predominantly* be present in the signal, with some rare events where it disappears. In this case, the *mean* amplitude \bar{A}_i would be close to the *saturated* value A_{is} , and even small instantaneous fluctuations around A_{is} would enhance artificial transitions from present to absent. Threshold values are increased by +29% for mode f_1 , by +47% for mode f_2 . It follows $\eta_1 = 0.376$ (−29%) and $\eta_2 = 0.283$ (−41%), $\eta_{\text{together}} = 0.15\%$, $\eta_{\text{none}} = 34.2\%$. The disproportion between η_{together} and η_{none} is dubious. Actually, in Fig. 8 is plotted the longest time interval, over which no mode should be present in the signal, following this criterion. This confirms that the criterion tends to overestimate the rate of common absence, which therefore appears rather irrelevant here.

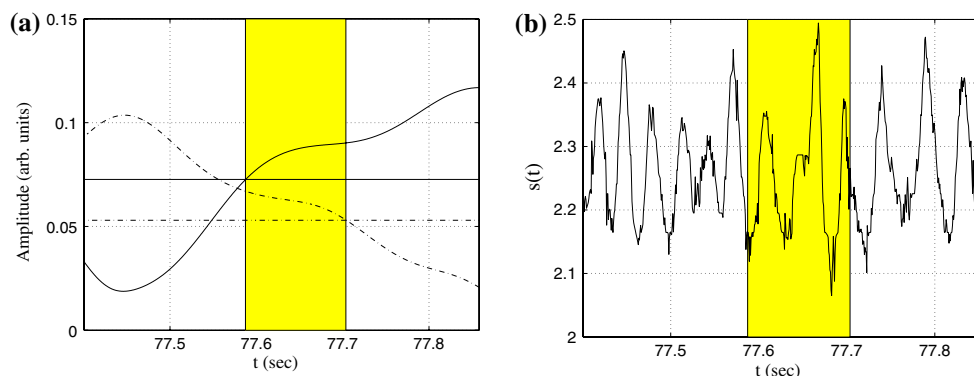


Fig. 7 Time range over which both modes are simultaneously present in the signal $s(t)$, following the criterion based on the mean amplitudes \bar{A}_1 and \bar{A}_2 . Mean amplitudes are plotted as *horizontal solid*

line for \bar{A}_1 and *broken line* for \bar{A}_2 . The common range is *grey filled*. **a** Amplitudes $A_1(t)$ and $A_2(t)$ are shown; **b** signal $s(t)$ is shown

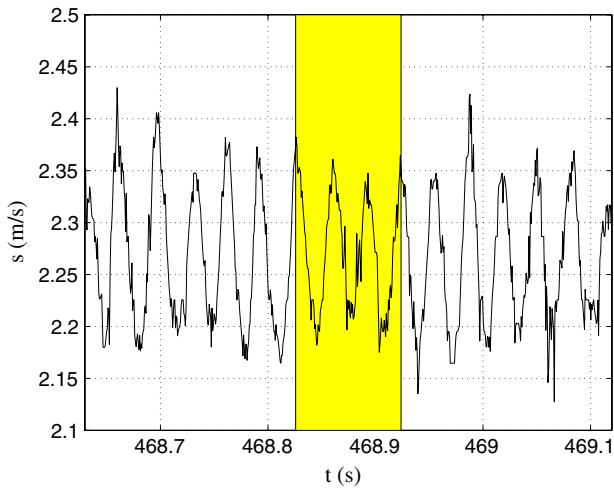


Fig. 8 In between *solid lines*, longest time range over which neither mode f_1 nor mode f_2 are detected within the signal, following the threshold value defined by Eq. 5

Another threshold value can be defined, when considering the amplitude distributions of modes f_1 and f_2 in Fig. 9. Two maxima are separated by a local minimum. The first maximum is the vanishing amplitude A_{iv} of mode f_i . The second maximum is the saturated amplitude A_{is} . The transition between the vanishing and the saturated amplitudes occurs when the amplitude passes through the local minimum A_{im} , which can provide a new threshold amplitude:

$$A_{im} = \min_{A_i \in [A_{iv}, A_{is}]} A_i. \tag{6}$$

If so, $A_{1im} = 0.060$ (−18%), $A_{2im} = 0.050$ (−6%). It follows $\eta_1 = 0.598$, $\eta_2 = 0.501$, $\eta_{together} = 13.0\%$, $\eta_{none} = 3.1\%$. Figure 10 shows the longest event for which both modes are simultaneously seen present in the signal. We will see in Sect. 7 that a similar criterion can be used, based on the system phase portrait.

Whatever criterion is used, η_1 is always greater than η_2 , already suggested by the PSD ratio between f_1 and f_2 , and the constraint $\eta_1 + \eta_2 + \eta_{none} - \eta_{together} = 1$ is always satisfied (see Table 1). The mean and maximum mode

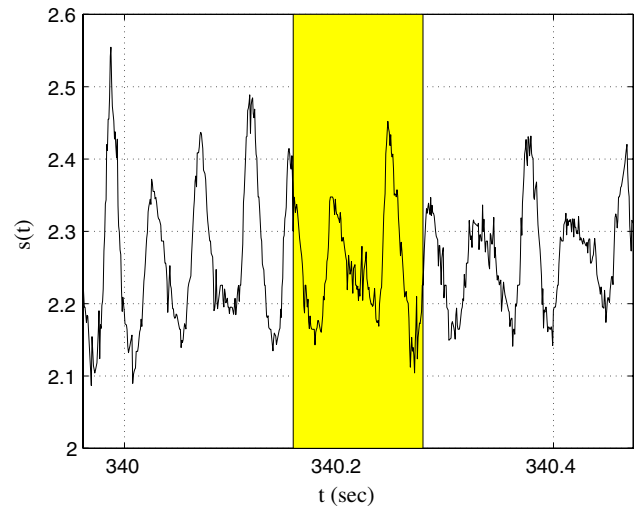


Fig. 10 Longest time range over which both modes f_1 and f_2 are detected in the signal $s(t)$, following the threshold value defined by Eq. 6

Table 1 Rate of existence η_1 (mode 1) and η_2 (mode 2), rate of coexistence of both modes η_{tgh} ($\eta_{together}$), rate of absence of both modes η_{non} (η_{none}), depending on the chosen threshold value (in %)

	η_1	η_2	η_{tgh}	η_{non}
Mean value \bar{A}_i	52.4	47.9	6.8	6.5
Mid-value A_{ic}	37.6	28.3	0.1	34.2
Local minimum A_{im}	59.8	50.1	13.0	3.1

Table 2 Mean lifetimes for modes f_1 and f_2 , depending on the chosen threshold value

	\bar{A}_i	A_{ic}	A_{im}
$\bar{\Delta t}_1$ (T_1 units)	19.6	12.0	24.7
$\bar{\Delta t}_2$ (T_2 units)	18.3	11.1	20.0

lifetimes are given in Tables 2 and 3, respectively. Short lifetimes are collected in Tables 4 and 5 for modes f_1 and f_2 . Lifetimes of common absence or presence are reported

Fig. 9 Amplitude distribution for (a) mode f_1 , (b) mode f_2 , using the Hilbert transform filter

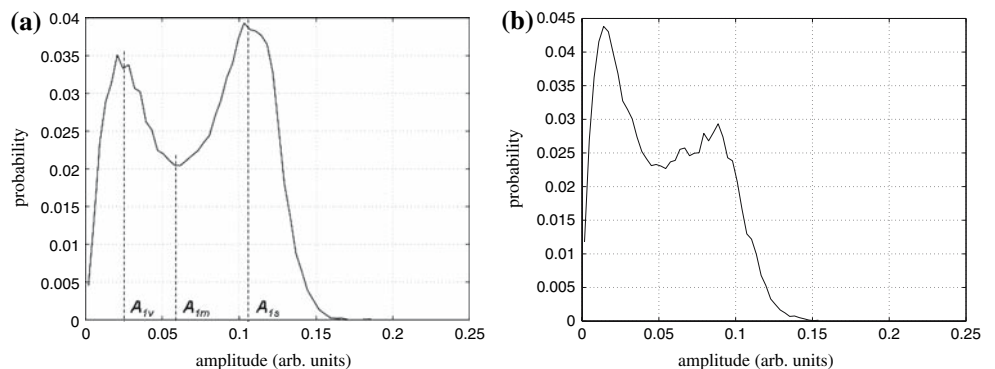


Table 3 Longest lifetimes for modes f_1 and f_2 , depending on the chosen threshold value

	\bar{A}_i	A_{ic}	A_{im}
Max Δt_1 (T_1 units)	408	238	454
Max Δt_2 (T_2 units)	509	211	511

Table 4 Nonrelevant lifetimes Δt_1 for mode f_1 depending on the chosen threshold value

	\bar{A}_1	A_{1c}	A_{1m}
Min Δt_1 (T_1 units)	0.27	0.31	0.23
Fraction of $\Delta t_1 < 2T_1$	6.3%	8.3%	9.7%

Table 5 Nonrelevant lifetimes Δt_2 for mode f_2 depending on the chosen threshold value

	\bar{A}_2	A_{2c}	A_{2m}
Min Δt_2 (T_2 units)	0.16	0.55	0.14
Fraction of $\Delta t_2 < 2T_2$	7.9%	12.5%	10.1%

Table 6 Time ranges over which both modes are either simultaneously present or absent from the signal

	\bar{A}_i	A_{ic}	A_{im}
Max $\Delta t_{\text{together}}$ (T_1 units)	12.3	2.5	17.1
Max Δt_{none} (T_1 units)	10.5	29.9	7.2
$\bar{\Delta t}_{\text{together}}$ (T_1 units)	1.9	0.8	2.7
$\bar{\Delta t}_{\text{none}}$ (T_1 units)	2.1	4.9	1.8
Fraction of $\Delta t_{\text{together}} < 2T_1$	62.2%	96.0%	46.9%
Fraction of $\Delta t_{\text{none}} < 2T_1$	56.9%	24.7%	64.3%

in Table 6. Time intervals whose duration are less than two basic oscillations may be considered as signal processing artifacts. Whatever threshold value is used, such events however represent less than 10% of the overall lifetimes for mode f_1 (Table 4), and not more than 13% for mode f_2 (Table 5). From Tables 4, 5, and 6, the mean amplitude seems to be the well adapted criterion here.

Depending on the criterion used, rates of existence sensibly vary. This is a consequence of the fact that the chosen threshold amplitude is to some extent arbitrarily defined. Moreover, we are facing the intrinsic limitation of any Fourier-based technique, where there exists a fundamental uncertainty over the time precision and where windowing usually introduce oscillations. The Hilbert transform, here based on band-pass filtered signals, extracts amplitudes that never vanish completely, even when one mode seems to be absent from the LDV signal. One may therefore ask whether this could result from

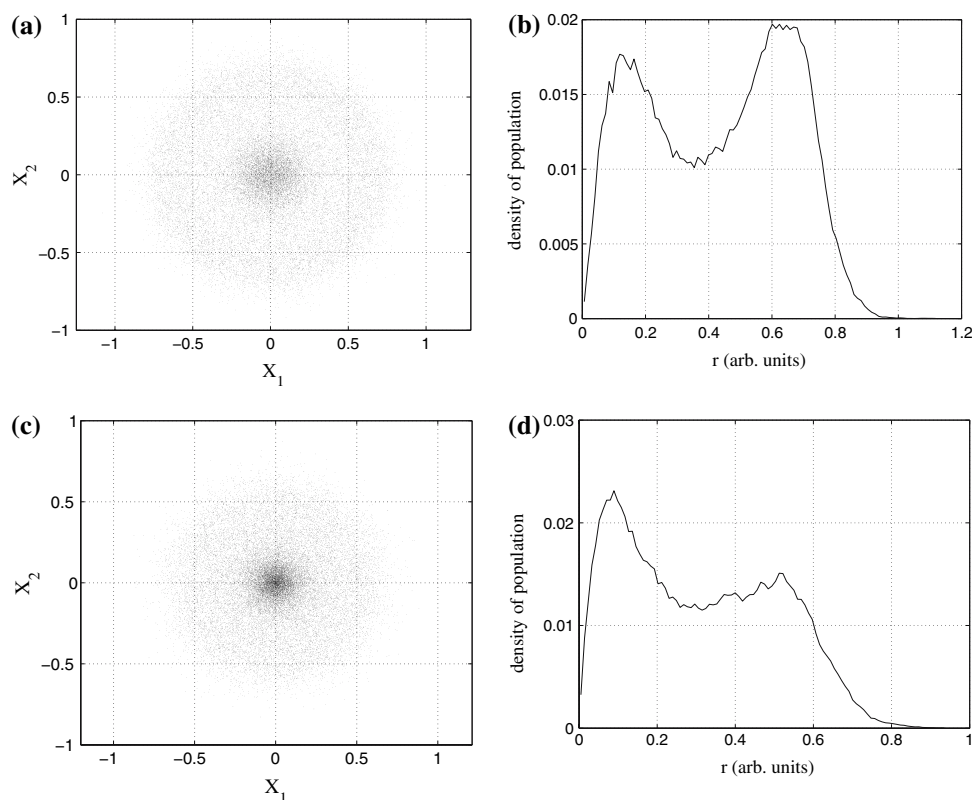
some processing artifact. However, a similar behaviour is observed in coupled complex Ginzburg–Landau equations, where two modes are similarly competing, and none never totally disappears. We have shown that none of the criterions introduced here, although justified by some aspects, looks fully satisfying, all being in some way arbitrary. Each of them however tells us that the coexistence or simultaneously absence of the two modes cannot be excluded, not only during events where both modes are exchanging stability, but also on reasonably long time durations (a few periods of oscillations for instance in Fig. 14a).

7 Phase space-based criterion

The phase space reconstruction is based on the singular value decomposition (SVD) of the delayed data matrix S , as proposed in Broomhead and King (1986). The SVD technique is described in Appendix. Derivative-based techniques would also generate an equivalent embedding phase space (Gouesbet and Letellier 1994).

Another threshold amplitude for the mode existence, similar to the one defined by Eq. 6, can be defined in the reconstructed phase spaces of the band-pass filtered signals $s_1(t)$ and $s_2(t)$. Let X be the matrix whose columns X_i are the phase space dynamical variables (see Appendix for the definition of X). Suppose that two columns of X , say X_1 and X_2 , are phase-quadratically correlated, as it is expected in an oscillating phenomenon. Then, X_1 is related to X_2 as would $s_1(t)$ be with respect to its first time-derivative $\dot{s}_1(t)$. For the sake of simplicity, consider the sub-phase space spanned by (s_1, \dot{s}_1) . Time ranges where both the amplitude and its time-variations are small will correspond to states close to the origin of the phase space (zero amplitude, zero derivative). On the contrary, time ranges over which the mode f_1 is present produce, in the signal $s_1(t)$, high amplitude levels (with a carrier time-varying at a frequency close to f_1), that generate orbits of finite radius $r(t) = \sqrt{s_1(t)^2 + \dot{s}_1(t)^2}$, with a significant dispersion if the amplitude modulations are large (Fig. 11a, c), further increased by the presence of noise. Between those two very distinct clouds of points should stand a “switching” area, associated with sharp amplitude falls (resp. rising) from the saturated (resp. vanishing) amplitude to the vanishing (resp. saturated) amplitude. Such front-like shaping in $A_1(t)$ occurs over time intervals where f_1 passes from being present (amplitude close to its saturated value), to absent (amplitude close to zero) in the signal (resp. from absent to present). Plotting the fraction of points as a function of their distance to the origin (Fig. 11b, d), it is observed two maxima, one at $r_{\text{inf},1} \simeq 0.14$, the other at $r_{\text{sup},1} \simeq 0.63$ for f_1 .

Fig. 11 **a** Phase portrait of the filtered signal $s_1(t)$, generated by applying the SVD to $s_1(t)$, as defined by Eq. 9. The two axes are the first two columns X_1 and X_2 of the matrix X , as defined by Eq. 10. **b** Radius distribution in the phase space. Each class of radius covers a $\Delta r = 0.01$; **c** idem to **a**, and **d** idem to **b**, for mode f_2



The first maximum is associated with the *vanishing* radius [when f_1 is absent from $s_1(t)$], the second maximum to the *saturated* radius. In between stands a relative minimum at $r_{0,1} \simeq 0.37$, which may be considered as the core of the transitory area, and may provide a new threshold amplitude. Next, the phase portrait distance

$r(t) = \sqrt{(X_1(t) - \bar{X}_1)^2 + (X_2(t) - \bar{X}_2)^2}$, of a point at time t with respect to the phase portrait centre, has to be compared with $r_{0,1}$. If $r(t) > r_{0,1}$, the mode is present in the signal, at time t , and absent otherwise. Noting n_1 the number of points in the phase space that fulfil the criterion, one can define the rate of presence of mode f_1 in the signal $s(t)$ as $\eta_1 = n_1/N$, N being the overall number of points. The same is done for f_2 , defining its rate of presence η_2 . One finds, in its associated phase portrait, $r_{\text{inf},2} \simeq 0.09$, $r_{\text{sup},2} \simeq 0.51$, and $r_{0,2} \simeq 0.30$. Applying the criterion, it comes $\eta_1 = 0.56$ and $\eta_2 = 0.46$. It is also found that both modes are simultaneously present in the LDV signal over 7.3% of T , while they are simultaneously absent from the signal over 6.0% of T . Rather surprisingly, the criterion gives results closer to those obtained when using the mean amplitude criterion, although it was expected to be more similar to the threshold value defined by Eq. 6. Note that the procedure may also introduce oscillations at $2\omega_1$ in $r(t)$, at least when $X_1(t) = \rho_1(t)\cos(\omega_1 t)$ and $X_2(t) = \rho_2(t)\sin(\omega_1 t)$, with $\rho_1 \neq \rho_2$, which might usually be the case (see Fig. 12).

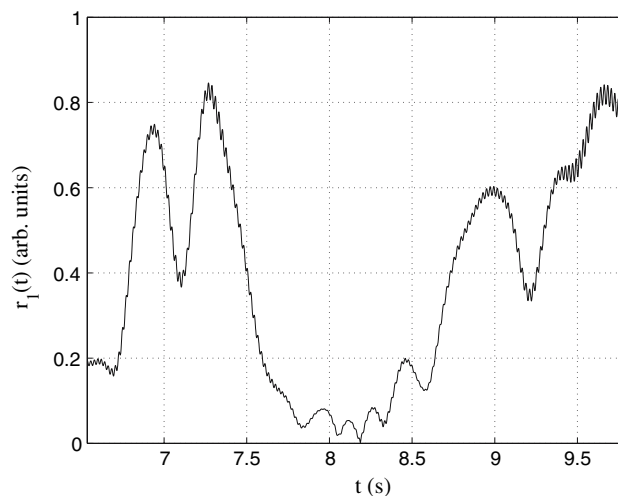


Fig. 12 Radius in the phase space, defined as $r(t) = \sqrt{(X_1(t) - \bar{X}_1)^2 + (X_2(t) - \bar{X}_2)^2}$, versus time, here for the mode f_1 . Small amplitude, high frequency oscillations at $2f_1$, can be seen on the slowly varying radius dynamics

8 Burst lifetime statistics

In what follows, the analysis is based on the threshold value defined by the time averaged amplitude. A sequence of events where both modes become simultaneously present or absent from the signal $s(t)$ is shown in Fig. 13 (grey

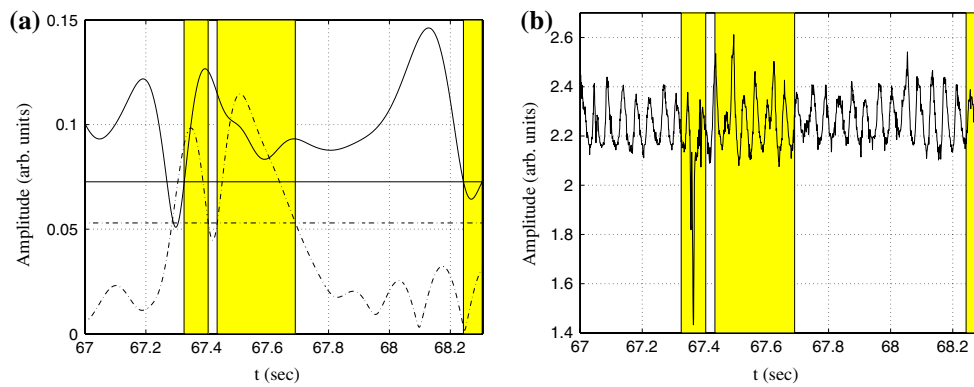


Fig. 13 Sequence of events where both modes become either simultaneously present or absent from the signal, (a) for the amplitudes, (b) for the signal $s(t)$. Such events are coloured in grey

bands. Left-hand and middle bands: both modes are present; right-hand band: both modes are absent. The threshold mean amplitude is shown as *horizontal line* in (a); *solid* for \bar{A}_1 , *broken* for \bar{A}_2

filled bands). The longest durations of simultaneous absence or presence are shown in Fig. 14.

Both mode lifetime distributions exhibit an exponential-like decay (Fig. 15), with a characteristic time duration $\tau_1 = 650$ ms for f_1 , $\tau_2 = 615$ ms for f_2 . The mean lifetimes are found to be $\bar{\Delta t}_1 = 795$ ms for mode f_1 (corresponding to about 20 cycles of basic oscillations at f_1), and $\bar{\Delta t}_2 = 545$ ms for mode f_2 (corresponding to about 18 cycles of basic oscillations at f_2). The longest lifetimes of each mode is found to be of the order of 5 s.

Similarly, the common time of presence or absence distributions are plotted in Fig. 16.

The successive n lifetimes $\{\Delta t_i^{(n)}, n = 1, 2, \dots\}$ of mode f_i , $i = 1, 2$, are plotted with respect to the $(n - 1)$ th lifetime in Fig. 17. In Fig. 18 is plotted the recurrence time of a mode, *ie* the elapsed time $\Delta\tau_{(k+1)}$ between two risings of the mode f_i in the signal with respect to $\Delta\tau_k$. From Figs. 17, 18, a deterministic law underlying the mode-switching phenomenon does not clearly appear, and a phase space analysis might help.

9 Phase space analysis

We now come back to the phase space reconstruction introduced in Sect. 7. The SVD is now applied to the original signal $s(t)$. It provides the matrix X defined in Appendix. Using a Grassberger Procaccia algorithm to estimate the phase space dimension (Grassberger and Procaccia 1983), it is found that the correlation dimension dynamics of the LDV signal $s(t)$ is of the order of 4.2, which means that the actual phase space dimension would at most be 10. Consequently, the number of coordinates required out of X is at most ten. The 2D projections of the phase portrait, in the planes (X_1, X_2) and (X_2, X_3) , are shown in Fig. 19a, b, respectively. The phase portrait is composed of a torus-like trajectory in a plane (almost) coplanar to the plane (X_2, X_3) , and exhibits transverse excursions in the X_1 direction.

To gain insights, a Poincaré section (Π) is defined by $\Pi = \{X_1, X_3 \in \mathbb{R}^2 | X_3 = 0, X_2 < 0\}$. (7)

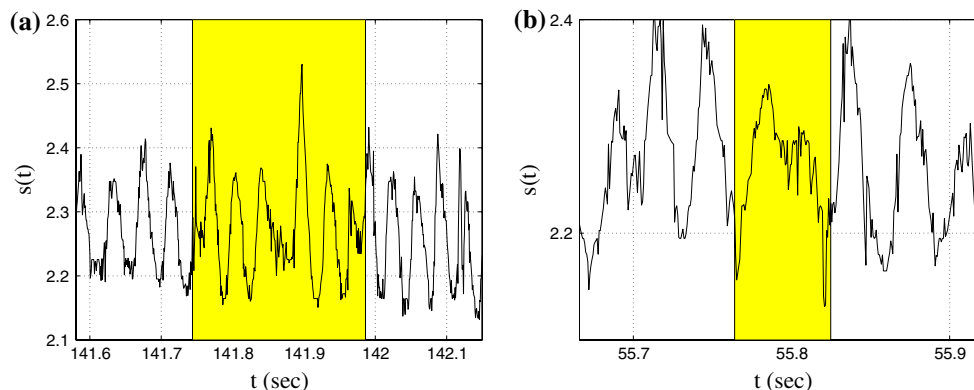


Fig. 14 Longest time of simultaneous (a) presence, (b) absence, of modes f_1 and f_2 in the signal, following the criterion based on the time averaged amplitude

Fig. 15 Life time distribution (a), (b) for mode f_1 , (c), (d) for mode f_2

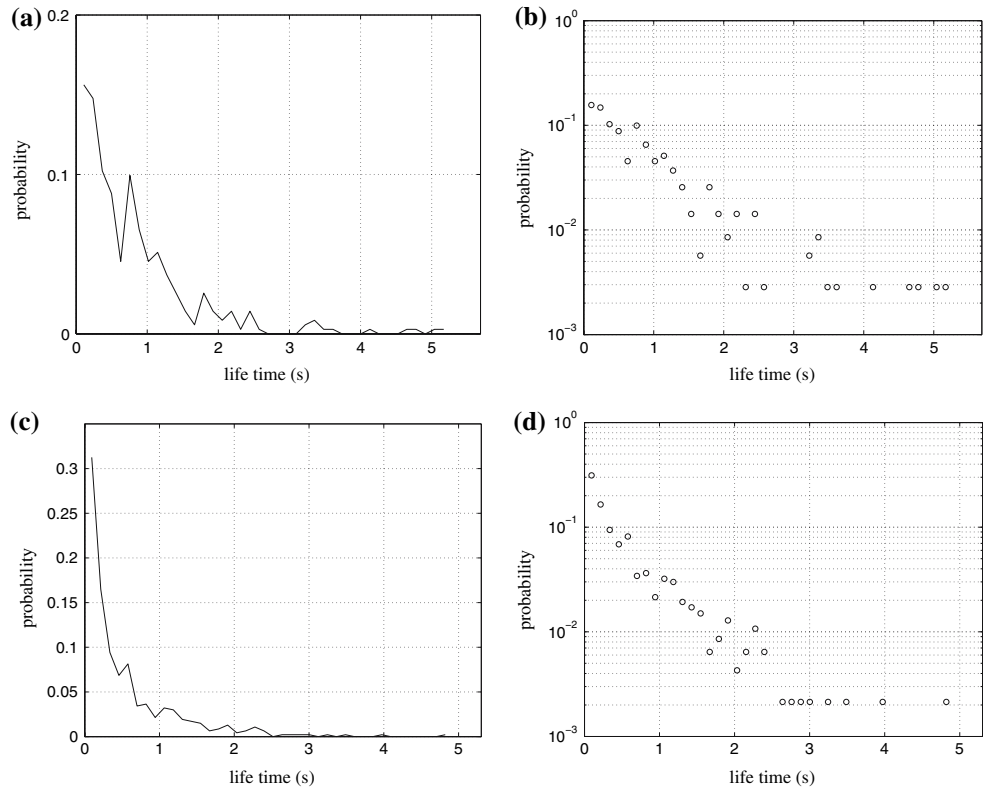


Fig. 16 Common time range distributions of (a) presence or (b) absence of both modes in the signal. The threshold amplitude is defined by the time-averaged amplitude

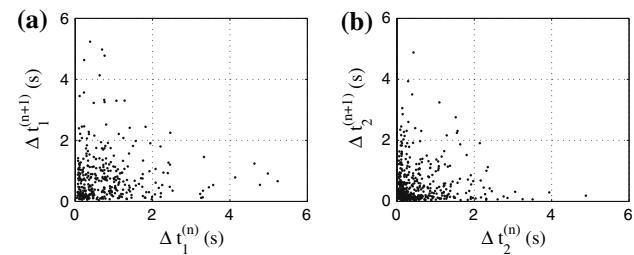
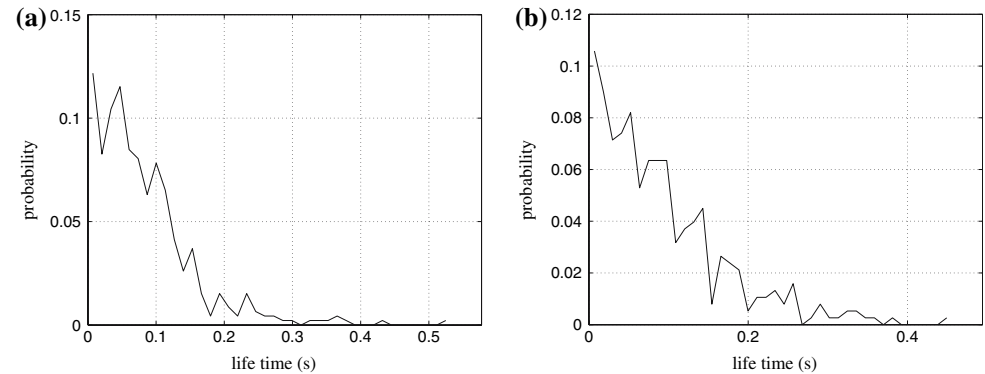


Fig. 17 $(n + 1)$ th lifetime of mode (a) f_1 , (b) f_2 with respect to the n th one

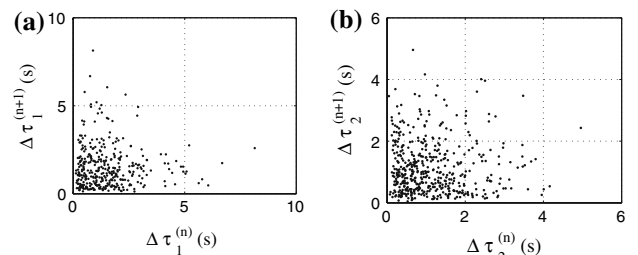


Fig. 18 $(n + 1)$ th cycle of rising/disappearance of mode (a) f_1 , (b) f_2 in the signal with respect to the n th one

The resulting Poincaré section is shown in Fig. 20. It exhibits two intricate clouds of points, each corresponding to the intersections of the (Π) plane with either the orbits at f_1 or f_2 (represented in two different colours). Points P_1 and

P_2 are the barycenters of the set of orbits associated with the modes f_1 and f_2 , respectively. Their coordinates, in the 10D reconstructed phase space, are:

Fig. 19 Phase portrait of $s(t)$, (a) in the (X_1, X_2) projection of the phase space (see Appendix for a description of matrix X), (b) in the (X_2, X_3) projection of the phase space

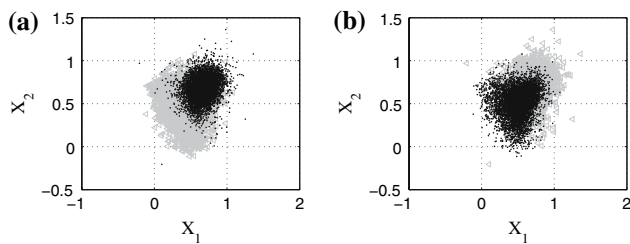
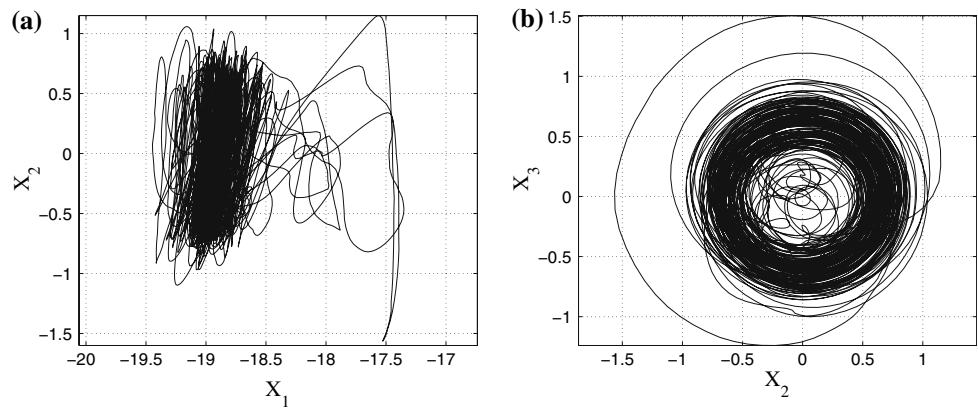


Fig. 20 Poincaré section (Π) , as defined by Eq. 7. **a** Dark points are the (Π) intersections with mode f_1 , grey points are the (Π) intersections with mode f_2 , **b** colours are inversed with respect to the previous case

$$P_1(-18866, 673, -31, -64, -13, 74, 37, -21, 24, 7.3) \times 10^{-3}$$

$$P_2(-18780, 509, -28, -15, -156, 39, 10, -22, -4, 6) \times 10^{-3}$$

Both barycenters are very close, which is coherent with the fact that orbits corresponding to modes f_1 and f_2 are closely intricate. In case there would exist two different attractors, each associated with each mode of oscillations, then the transition from one attractor to the other might be very easy, their basin of attraction presumably being intricate as well. In another case, the dynamics could evolve over one unique attractor. From the Hilbert analysis (see Fig. 7) and the power spectrum of Fig. 2, none mode never completely disappears from the signal (background level), since it can be seen from Fig. 15 that amplitudes $A_{1,2} = 0$ are very unlikely. Therefore, the dynamics should essentially evolve over a torus, whose section would most of the time be pretty elliptic, since one of the two amplitudes is usually small when the other is saturated. The phase space trajectories would essentially be orbits cycling along the torus, at the frequency of the strongest mode. At some time, mode predominance is exchanging, and the torus main extension would become the saturated amplitude of the other mode, while orbits would now evolve at the new frequency.

10 Conclusion

The self-sustained oscillations observed in open flows may present a very rich phenomenology. In the case of a fluid flowing above an open cavity, here at a moderate Reynolds number ($Re_L \approx 14,000$), for an aspect ratio $R = 2$, the nonlinear competition between noncommensurable modes of oscillations reveals to be essentially dominated by a mode-switching scenario. It is however shown, following any criterion introduced in this paper, that a non-negligible fraction of time can be found, where both modes may simultaneously be present in, or absent from the flow oscillations.

Working in the phase space, it might be possible to introduce another criterion based on a first-return map built on the Poincaré section. Would the resulting symbolic dynamics have any sense with respect to the mode-switching phenomenon, it would be possible to define an absolute criterion, whose time-precision would be at the scale of the orbit duration (impact through the Poincaré section). A deeper study of the symbolic dynamics, though out of the scope of this paper, would therefore be interesting to investigate, possibly revealing the mechanisms responsible for the exchange of stability between the two modes.

The spatial flow structure is controlled by the length and height of the cavity, and by the lateral (rigid) boundary conditions (Faure et al. 2007). The later are suspected to play a key role in the nonlinear mode competition observed in the shear layer oscillations. Further investigations are necessary. Hopefully, 3D direct numerical simulations of the flow, in the condition of the experiment, should advantageously help understanding the fine interaction between the spatial structure dynamics, and the shear layer time dynamics. It is known that modifying Re_L will also modify the excited mode frequencies in the shear layer, their relative amplitude in the spectrum, and modifies their rates of existence as well as the fraction of common times (Faure et al. 2005).

11 Appendix: Phase portrait based on a singular value decomposition

The method for reconstructing an embedding phase space is based on the singular value decomposition (SVD) of the matrix S of the delayed data, built from the LDV signal $s(t)$ as

$$S = \begin{pmatrix} s(t_1) & s(t_2) & \dots & s(t_m) \\ s(t_2) & s(t_3) & \dots & s(t_{m+1}) \\ \vdots & & & \\ s(t_{N-m+1}) & s(t_{N-m+2}) & \dots & s(t_N) \end{pmatrix}. \quad (8)$$

Matrix S is of size $m \times N$. Times $t_k = t_{1+k} \delta t$, $k \in \mathbb{N}$, are defined with respect to the initial acquisition time t_1 , with $\delta t = 0.65$ ms. Henceforth, one period of the basic cycle contains about $m = 70$ points. The SVD procedure then identifies the singular vectors of the matrix S (and its associated singular values), which correspond to the proper “deterministic” axes of the matrix. The singular vectors are ranked as columns of a matrix V_S such that

$$S = U_S \cdot D_S \cdot V_S^T, \quad (9)$$

where D_S is the $m \times N$ matrix of the singular values (ranked from the largest to the smallest one). Note that S is most usually not a square matrix, and therefore most of its singular values vanish. In fact, $N \gg m$, and therefore $(N - m) \gg 1$ singular values are equal to zero. Consequently, it has no sense to compute all the singular values and singular vectors of S , since only m of them are dynamically relevant. The time-delayed system S is then projected onto its singular basis, namely, V_S , through the matrix product $S \cdot V_S$. The matrix V_S being orthogonal, it follows that $V_S^T \cdot V_S$ is the identity matrix, and therefore $S \cdot V_S = U_S \cdot D_S$. Henceforth, the searched out phase space may be spanned by the columns of the matrix X , defined as

$$X = U_S \cdot D_S. \quad (10)$$

References

- Broomhead D, King G (1986) Extracting qualitative dynamics from experimental data. *Physica D* 20:217–236
- Faure TM, Debesse P, Lusseyran F, Gougat P (2005) Structures tourbillonnaires engendrées par l’interaction entre une couche limite laminaire et une cavité. In: 11ème Colloque de Visualisation et de Traitement d’Images en Mécanique des Fluides, IUTAM, Lyon, France, pp 6–9
- Faure T, Adrianos P, Lusseyran F, Pastur L (2007) Visualizations of the flow inside an open cavity at medium range reynolds numbers. *Exp Fluids* 42:169–184
- Gadoin E, Quéré PL, Daube O (2001) A general methodology for investigating flow instability in complex geometries: application to natural convection in enclosures. *Int J Numer Methods Fluids* 37:175–208
- Gouesbet G, Letellier C (1994) Global vector-field reconstruction by using a multivariate polynomial l_2 approximation on nets. *Phys Rev E* 49:4955–4972
- Grassberger P, Procaccia I (1983) Characterization of strange attractors. *Phys Rev Lett* 50:346–349
- Kegerise M, Spina E, Garg S, Cattafesta L (2004) Mode-switching and nonlinear effects in compressible flow over a cavity. *Phys Fluids* 16:678–687
- Le Quéré P, Masson R, Perrot P (1992) A Chebyshev collocation algorithm for 2D non-Boussinesq convection. *J Comput Phys* 103(2):320–335
- Leonard BP (1979) A stable and accurate convective modelling procedure based on quadratic upstream interpolation. *Comput Methods Appl Mech Eng* 19:59–98
- Podvin B, Fraigneau Y, Lusseyran F, Gougat P (2006) A reconstruction method for the flow past an open cavity. *J Fluids Eng* 128:531–540. doi:10.1115/1.2175159
- Rockwell D (1983) Oscillations of impinging shear layers. *AIAA J* 21(5):645–664
- Rockwell D, Naudascher E (1979) Self-sustained oscillations of impinging free shear layers. *Annu Rev Fluid Mech* 11:67–94